

Investigating Moiré Physics in 2D heterostructures using EMPAD detector:

A study of Charge Density Mapping

Sangers, J. (4645197)
Applied Physics - Master Thesis
TU Delft
18th September 2023

Abstract

Contents

Table of Contents	ii
1 Introduction	1
2 Theory	2
2.1 The Transmission electron microscope	2
2.1.1 Bright Field	3
2.1.2 Dark Field, Z-contrast	3
2.1.3 Energy-dispersive x-ray spectroscopy	5
2.2 TMDC/Crystal structure	5
2.2.1 Transition metal dichalcogenides	5
2.2.2 Crystal lattice and band structure	5
2.2.3 Reciprocal lattice and electron diffraction	6
2.2.4 Convergent beam electron diffraction	7
2.3 Moiré Physics in two-dimensional heterostructures	7
2.3.1 Diffraction pattern and Brillouin zones of moiré heterostructures	8
3 Fabrication of two-dimensional moiré heterostructures	9
3.1 Exfoliation of monolayer material	9
3.2 Verification of monolayer material	9
3.3 Assembling a heterostructure	11
3.4 Transferring to a TEM grid	12
4 Advanced electron microscopy techniques to map moiré physics at the nanoscale; an electron microscope pixelated array detector.	13
4.1 Electron microscope pixel-array detector	13
4.2 Strain analysis	14
4.2.1 Micrometer field-of-view strain analysis	15
4.2.2 Nanometre field-of-view strain analysis	15
4.3 Ptychography	15
4.4 Charge density analysis	15
5 Case study of $MoSe_2/WSe_2$ moiré heterostructures	16
5.1 Verification of moiré pattern and its parameters	16
5.2 Analysis of in-plane strain	16
References	17

1 Introduction

1. use of tmdc, QComp, optoelec
2. flat bands

2 Theory

2.1 The Transmission electron microscope

The Transmission electron microscope (TEM) is a microscope that far exceeds the capabilities of a normal light microscope. Both types of microscope use a series of lenses to magnify the image of a specimen. A normal light microscope can amplify an image up to about $1500\times$ and is limited by the diffraction limit of light. Assuming an average wavelength of 550 nm for green light, a high-end microscope is limited to resolving features 100 nm apart. This limit is insufficient for looking at atomic structures [1].

An electron microscope circumvents this limit by using electrons, not light, to probe the specimen. Electrons when accelerated have a smaller wavelength than light thus allowing for images with resolved features as small as 0.05 nm. [2] The TEM works by releasing electrons from an electron source and accelerating them to an energy typically expressed in kilo-electronvolt; as shown in equation 1, the higher the accelerating voltage of the microscope the smaller the de Broglie wavelength of an electron, which results in a higher resolving power. Modern electron microscopes accelerate electrons up to 300 keV

$$\lambda_e = h \cdot [2 \cdot e \cdot m_e \cdot V_a]^{-1/2} \quad (1)$$

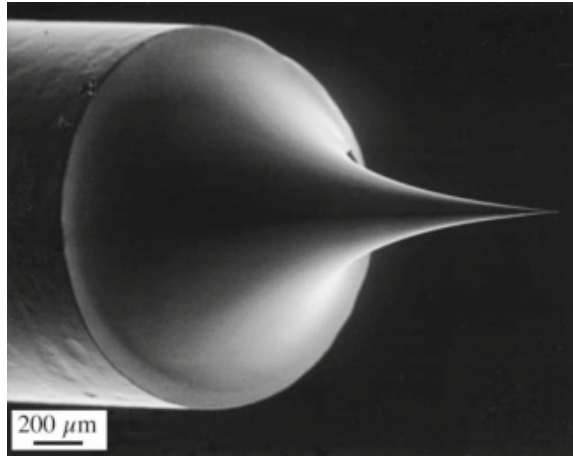


Figure 1: Pictured is the tip of a field emission gun [3]. The tapered tip facilitates the creation of a strongly varying potential that eases the expulsion of electrons from the material. These electrons are then accelerated along the optical axis.

In a TEM the electrons are released from a field emission gun (FEG, pictured in Figure 1). The FEG is placed in proximity to two anodes, the first anode is positively charged to several kilovolts such that it extracts electrons from the tip of the FEG, the second anode is charged to the wanted acceleration voltage [3]. FEGs are about three orders of magnitude brighter than thermionic emission electron sources [4]. After being emitted the electrons pass through a monochromator that reduces the energy spread of the emitted electrons. An electron then continues along the optical axis into an illuminating system consisting of multiple electromagnetic lenses, which lenses are activated and to what extent depends on the operating mode of the electron microscope.

2.1.1 Bright Field

A bright field (BF) image of the sample is acquired by using a parallel electron beam. This beam is formed using the lens configuration shown in figure 2. This parallel beam is typically several micrometers in size at magnifications up to 20k-100k \times . In normal operating mode a BF image is captured by a camera looking at a phosphorous screen or by a camera directly, this method of imaging is most analogous to a normal light microscope. The electron beam is focused in such a way that it illuminates the sample with a parallel beam, such a beam is also used for creating the clearest diffraction patterns.

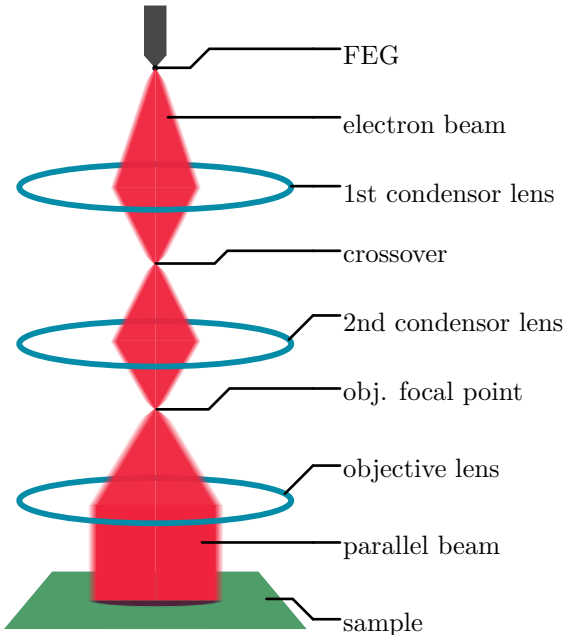


Figure 2: Illumination system for parallel beam.

2.1.2 Dark Field, Z-contrast

For dark field and Z-contrast the electron beam is focused to a small area, this creates a higher intensity electron beam with a probe-like point as can be seen in Figure 3. Since all the electrons are focused on a small area there is no contrast information that can be used to form an image. To form an image using such a beam the probe point needs to be scanned over the sample leading to the term Scanning Transmission Electron Microscopy. Dark field images use electrons scattered away from the optical axis to form an image, to achieve this most STEMs have a series of annular dark field detectors. These ring shaped detectors encircle the central bright field detector and can collect electrons that have been scattered at various angles. Normal dark field detectors collect electrons scattered up to an angle of 50 mrad. The outermost detector is the high-angle annular dark field detector (HAADF) which collects electrons scattered beyond 50 mrad and can be used to create Z-contrast (atomic number Z) or mass-thickness images. The HAADF detector is used since the electrons it collects are almost exclusively incoherently elastically scattered which is proportional to

the atomic number Z. The scanning beam then gathers this atomic number information as intensity information for every probe position in the sample. Layering two monolayers such that the atoms are aligned, and the probe is perpendicularly incident on the sample will sum the intensity of the two atomic weights of the stacked atoms in the image. The stacking pattern can then be determined by looking at a line plot of the atomic mass over atoms.

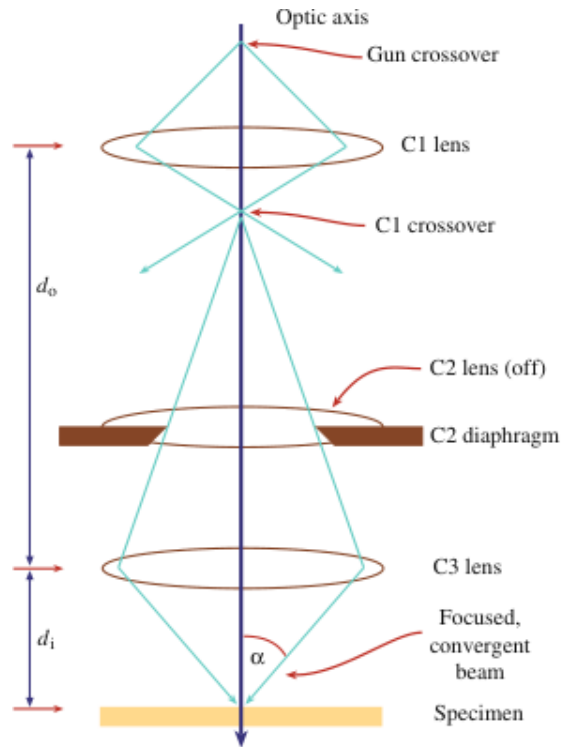


Figure 3: Illumination system for convergent beam.

2.1.3 Energy-dispersive x-ray spectroscopy

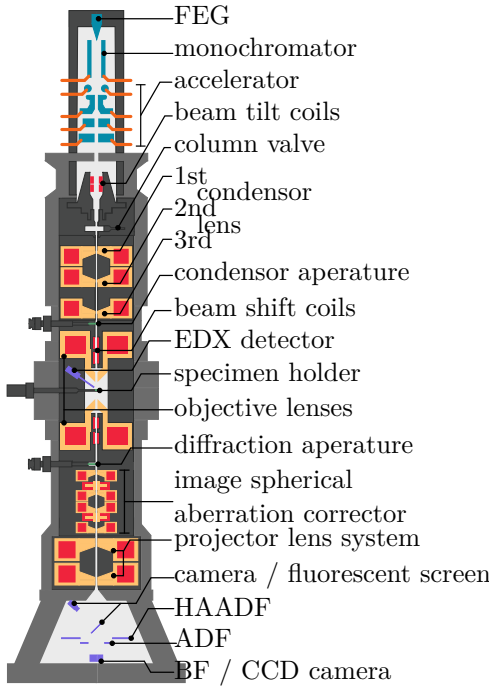


Figure 4: Cross-section of an aberration corrected electron microscope

2.2 TMDC/Crystal structure

2.2.1 Transition metal dichalcogenides

Transition metal dichalcogenides or TMDCs are a family of materials consisting of transition metals (group 3 through 12 on the periodic table) and chalcogen atoms (Sulphur, Selenium or Tellurium) in an MX_2 -configuration, where M is the metal atom and X_2 are the chalcogen atoms [5]. The properties of TMDCs depend greatly on the amount of stacked layers and with individual layers being as thin as 6.5 \AA for MoS_2 these materials are often referred to as layered or two-dimensional materials. Decreasing the amount of layers from bulk changes electrical properties such as the bandgap which for some TMDCs can go from an indirect to a direct bandgap. These electrical properties make TMDCs useful in electronics as transistors and in optoelectronics as emitters and detectors [6, 7, 8]. If present, multiple layers of TMDCs are held together by weak interlayer Van der Waals forces making these materials flexible and transferable using polymer based techniques [9].

2.2.2 Crystal lattice and band structure

An infinitely repeating group of atoms is called an ideal crystal, such a crystal is constructed by attaching the same group of atoms, often called a unit cell, to a lattice. The lattice can be

constructed from n independent lattice vectors. $n = 1$ for an atomic chain, $n = 2$ for a two-dimensional monolayer, and, $n = 3$ for a three-dimensional crystal. If no smaller repeating group of atoms can be constructed to fill the lattice then this group of atoms is called the primitive unit cell and the n -independent lattice vectors are then called the primitive translation vectors a_n [10]. Each of the n lattice vectors signifies a direction and length of displacement needed such that the shifted crystal lattice is indistinguishable from the original crystal lattice 2. Lattice vectors are also used to specify the orientation of a crystal plane by denoting where the plane intersects the lattice vectors, this procedure allows for unique indexing of crystallographic planes. The use of these planes will be discussed in 2.2.3.

$$\vec{r}' = \vec{r} + u_1\vec{a}_1 + u_2\vec{a}_2 + u_3\vec{a}_3 \quad (2)$$

2.2.3 Reciprocal lattice and electron diffraction

In the previous section the crystal lattice was introduced, and it was mentioned that there were unique planes characterized by the points where they intersect the lattice vectors. In reciprocal space every lattice point is equivalent to one set of these planes. To best understand a crystal, it is helpful to conceptualize it as having two lattices. The first lattice pertains to the organization of the atoms within the crystal's unit cells. The second lattice is a pattern of points that is specific to each crystal and does not correspond to the atom arrangement. Rather, each point in the lattice is linked to a particular set of planes within the crystal [3]. Both lattice constructions are equally valid but are helpful under different circumstances; the reciprocal lattice, for instance, is a useful geometrical construct when talking about diffraction.

The reciprocal lattice, just like the crystal lattice, is constructed by vectors; in the case for the reciprocal lattice these are the reciprocal lattice vectors \vec{b}_n . The reciprocal lattice vectors are constructed from the real-space lattice vectors using equation (3) and satisfy relation (4) with their real-space counterpart. Using these definitions the reciprocal lattice vectors are unique. Any reciprocal vector can now be composed uniquely by a linear combination of the reciprocal lattice vectors, such that any vector is scaled and summed. If the scalars are integers they are the miller indices and correspond to a crystallographic plane.

Scattering off of these planes shows as a series of high-intensity spots in a diffraction pattern image (Figure 5), such an image can be taken in the diffraction mode of a scanning transmission electron microscope (STEM).

$$\vec{b}_i = 2\pi\vec{a}_j \times \vec{a}_k \cdot [\vec{a}_i \cdot (\vec{a}_j \times \vec{a}_k)]^{-1} \quad (3) \qquad \vec{b}_i \cdot \vec{a}_j = 2\pi\delta_{ij} \quad (4)$$

In a transmission electron microscope the electrons emanating from the field emission gun are modelled as plane waves. When incident on an atomically thin crystalline sample, the plane waves scatter predictably following the physical criteria that incoming and outgoing electrons beams are plane waves with wave vectors \vec{k}_I and \vec{k}_O for incoming and outgoing waves. The resulting change in wave vector due to the scattering of the sample is then equal to $\vec{K} = \vec{k}_I - \vec{k}_O$. As seen in Figure 6, the outgoing electron beam wavefront is deflected by an angle θ from the incident electron beam such that both are in phase, this angle is the Bragg angle [3]; and using that $|\vec{k}_I| = |\vec{k}_O| = |\vec{K}| = \lambda_e^{-1}$, with λ_e the electron wavelength, the scattering angle can be expressed as:

$$\sin \theta = \frac{|\vec{K}|/2}{|\vec{k}_I|} \quad (5)$$

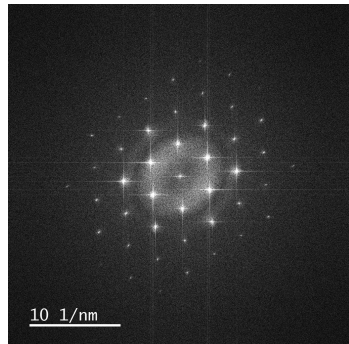


Figure 5: Diffraction Pattern

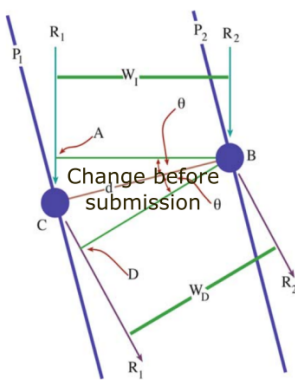


Figure 6: Scattering diagram

If both outgoing rays from the same incoming beam wavefront are then in phase, meaning that the extra distance travelled by one of the rays is a multiple of the wavelength, it shows as a bright spot in the image and then the following condition is met for the Bragg angle:

$$n\lambda_e = 2d \sin \theta_B \quad (6)$$

This shows that scattering allows for a finite quantized momentum transfer from the electron to the crystal lattice or vice versa. In a crystalline sample this results in bright spots in the diffraction image, where each bright spot can be indexed and attributed to a family of planes in the crystal that facilitate the momentum transfer for the electrons to reach that spot on the detector or phosphor film. Just as the real-space lattice has a unit cell so does the reciprocal lattice. In reciprocal space this unit cell is called the Brillouin zone.

2.2.4 Convergent beam electron diffraction

2.3 Moiré Physics in two-dimensional heterostructures

1. moire pattern -> stacking

2. lattice relaxation
3. mini brillouin zone / aligned or antialigned
4. hybridisation, inter/intra transistions and excitons
5. band bending types, umklapp, flat bands

2.3.1 Diffraction pattern and Brillouin zones of moiré heterostructures

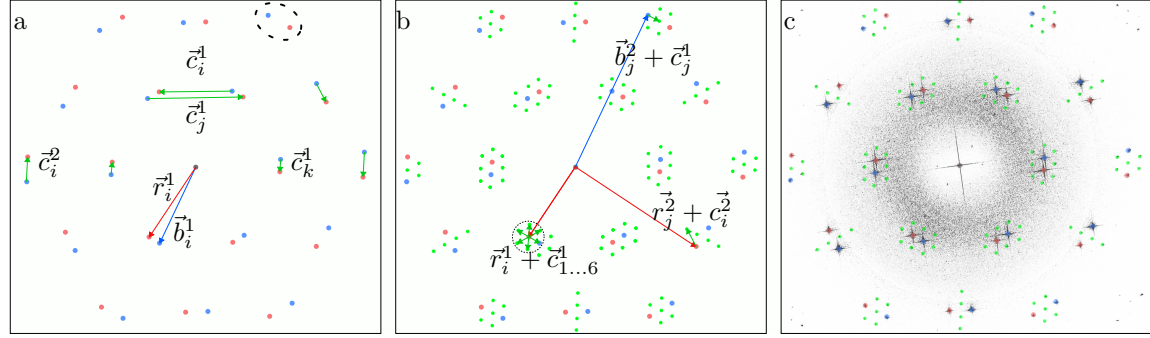


Figure 7: Overview of the global strain present in the heterostructure

3 Fabrication of two-dimensional moiré heterostructures

Mechanical transfer in this thesis relates to the practise of both the stamping of two monolayers on top of one-another to form a bilayer heterostructure and the transferring of that heterostructure from the substrate it was stamped on to the holey-carbon TEM grid for inspection in the electron microscope.

3.1 Exfoliation of monolayer material

For the preparation of the heterostructures, monolayer flakes were prepared using a three-step process. Firstly bulk crystal material was exfoliated between scotch tape two to three times, using the same method as often is used for graphene [11], to prepare fresh flakes. These fresh flakes would then be transferred to a Polydimethylsiloxane (PDMS) stamp by placing the PDMS stamp on the scotch tape with the flakes before quickly peeling the stamp off with tweezers. For this step it is important that the peeling speed is high as for PDMS the adhesion force to the flake is proportional to the peel-off speed [12]. Thirdly, the flakes present on the PDMS stamp were inspected using an optical microscope before being exfoliated using PDMS stamps. At this stage PDMS stamps are used for exfoliation as they provide a gentler way of further cleaving the bulk flakes as well as eliminating a further transfer step from tape to PDMS if a monolayer flake were to be exfoliated using tape since stamping on a substrate with tape is difficult. The exfoliation using two PDMS stamp is performed by laying the stamps on another while on a glass slide to provide support after which both stamps are peeled from the glass before separation by two tweezers. Both stamps are now inspected by means of an optical microscope, if monolayer (ML) material is present on either of the stamps it can later be used in creating a heterostructure. If no ML material is present on a stamp the third step can be repeated until there is ML material or the flakes have broken up into unusable small pieces. Furthermore, sacrificial or pristine PDMS stamps can be used to either remove unwanted small flakes or transfer large flakes to a newer and cleaner PDMS stamp, this selective transfer is performed under a microscope such that existing ML material can be avoided as this will likely break if exposed to the force caused by peeling away the sacrificial PDMS stamp.

3.2 Verification of monolayer material

lay. #	Photon Energy of Exciton [eV]	
	A	B
1	1.54	1.79
2	1.55	1.80
3	1.56	1.80

Table 1: Measurements of the dip positions for the A- and B-exciton in $MoSe_2$ flakes of varying layer thickness

lay. #	Photon Energy of Exciton [eV]		
	A	C	D
1	1.666	2.429	2.813
2	1.654	2.323	2.742
3	1.644	2.226	2.716
4	1.632	2.200	2.726
5	1.623	2.200	2.820
6	1.622	2.182	2.794

Table 2: Measurements of the dip positions for the A-, C- and D-exciton in light transmittance spectra of WSe_2 of varying thickness.

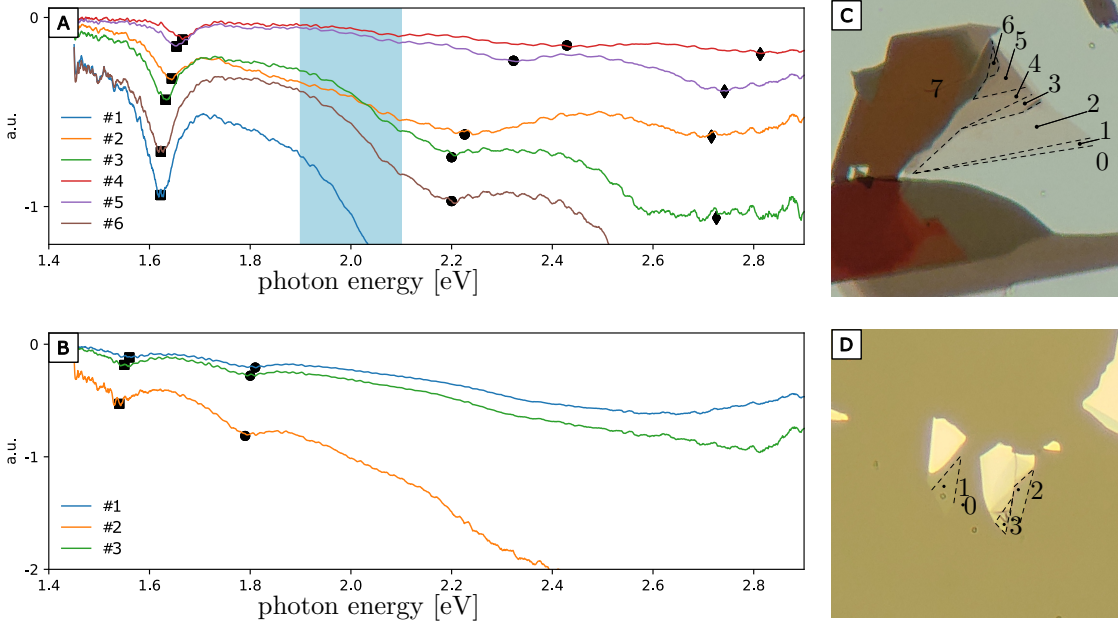


Figure 8: Transmittance spectra, recorded using a light spectrometer, of flakes of varying thicknesses. A) Transmittance spectra for 1 to 6 layers of WSe_2 exfoliated, using the previously described method, onto a PDMS on glass substrate. B) transmittance spectra of 1 to 3 layers of $MoSe_2$. C,D) The flakes used for the collecting the spectra of WSe_2 (A, C) and $MoSe_2$ (B,D) respectively. In A) the square, circular, and, diamond marker; denote the location of the peaks of the a - c - and, d -exciton of WSe_2 found by fitting to a linear combination of Lorentzian peaks. The shaded blue region denotes the photon energy range in which the b -exciton peaks is expected but not found by the fitting model. Similarly, in B) the square and circular marker denote the location of the a - and b -exciton peaks of $MoSe_2$.

Since the bandgap of TMDCs becomes direct in a single layer and most interesting moiré effects come into play for monolayer flake heterostructures its is important to determine the number of layers in the flakes that are used for heterostructures. For the first round of samples, optical inspection with a transmittance light microscope proved to be too crude to determine the layer number for flakes thinner than three layers. Solving this issue included setting up a new transmittance- and reflectance-mode microscope with a spectroscope attached, the whole set-up is copied from another lab and proven to be able to differentiate between amount of layers in a flake. [13, 14] Using this set-up transmittance- and reflectance-spectra were recorded for both WSe_2 and $MoSe_2$ flakes for varying layer numbers, the transmittance spectra are displayed in Figure 8A,B for both materials respectively. Even though both light sources used for transmittance and reflectance spectra in transmission and epi-illumination mode should be the same halogen bulbs, the reflectance spectra suffered from greater noise in the ≤ 1.6 eV range due to the lower intensity of light emitted by the epi-illumination bulb in this region. For this reason the reflectance spectra proved less suited to identifying flake thickness and are thus omitted from this work. All spectra were collected using a $100\times$ -magnification $0.55NA$ objective and $150\text{ }\mu\text{m}$ thick core glass fibre leading to the spectrometer. The spectrometer collected and averaged 50 spectra that were integrated over 500 ms. To improve the rejection of stray light, the field aperture of the light was closed fully. As can be seen in

the transmittance spectra, the overall intensity difference is the best indicator for flake thickness beyond 2 layers whereas the location of the A-exciton is the key differentiator between 1 or 2 layers. Using the spectroscope and the new microscope has greatly decreased the time required and greatly increased the ease of finding thin material and verifying its thickness.

3.3 Assembling a heterostructure

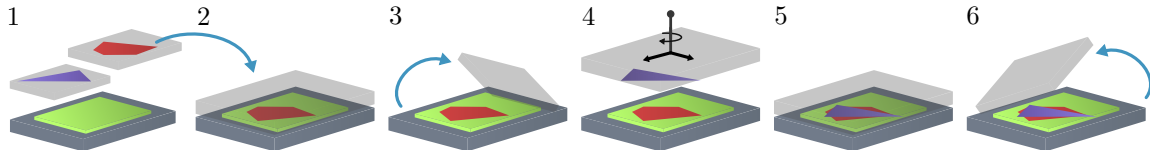


Figure 9: Schematic outline of the stamping process. 1: Before starting, two PDMS stamps with monolayer material and a silicon substrate coated with PVA should be prepared. 2: The first flake is stamped, preferably as close to the centre of rotation of the substrate stage as possible as this makes aligning the next flake easier. 3: The micromanipulator with the PDMS stamp is slowly raised to peel the PDMS stamp off of the substrate, leaving behind the first monolayer flake. 4: The second stamp with monolayer material is aligned by rotating the substrate stage and moving the stamping micromanipulator. 5: The stamp is then carefully lowered and misalignment is corrected if necessary. 6: The second stamp is removed slowly, and both flakes are transferred to the substrate.

Once two suitably matching monolayer flakes have been located on different PDMS stamps they can be assembled to form a heterostructure. The flakes are stamped onto a specially prepared substrate using a dedicated stamping set-up that allows for micrometer precise control over flake position and consists of two main parts: a substrate stage, and, a flake stage. The substrate stage has three degrees of freedom: two micromanipulators control the x - and y -position of the substrate under the microscope and the stage itself is free to rotate to align the edges of the to be stamped ML flakes. The stamping stage is capable of precisely moving a glass slide with a stamp along three axes. The complete stamping set-up is pictured in Figure ?? and is a direct adaptation from previously published set-ups [15, 16]. The stamping set-up consists of: a reflective optical microscope, a rotating substrate stage attached to two micromanipulators, and, a stamping stage connected to three micromanipulators. The ML material is stamped onto the substrate by first adhering the PDMS stamp onto a glass microscope slide and inserting this slide into a holding mechanism on the stamping stage, after which the stamp is carefully brought into contact with the substrate as illustrated in Figure 9. Since we wish for the flake to adhere to the substrate and not the stamp, we now slowly release the stamp from the substrate, the stamp peel-off speed is crucial at this step and should be as slow as possible without stopping the process. During this step of the process it is also paramount to not introduce any vibration or other forces as these can easily tear the flake. Applying the second stamp with ML material requires more care and effort as this stamp needs to be aligned with the first already stamped monolayer flake. The aligning step is performed by first locating the ML material on the substrate and then roughly aligning the micromanipulator with the second flake. Then experience has shown that the easiest way to proceed is by aligning the edges of both flakes to the desired angle as changing the angle of the flake on the substrate requires rotating the stage and most likely the stamped flake out of view. After alignment of the angles it is now possible to place the flakes above one-another using the micromanipulators. Slowly lowering the second stamp to the substrate will bring both flakes into view allowing for a more precise alignment, during further lowering of the flake its best to zoom out as to be able to see

where the PDMS stamp first contacts the substrate. If this first point of contact is too far from the ML material, further lowering of the stamp can squeeze the PDMS and cause the flake to move in the direction of the contact-front propagation during further lowering; if this happens restarting the stamping procedure and compensating for the movement is possible, but it is advised to remove the glass slide with the flake completely and cut the PDMS in such a way that the first point of contact is closer to the ML material. After stamping of the second flake is completed the PDMS needs to be slowly peeled off again in the same manner as before, after which the result will be a heterostructure on the prepared substrate, ready for transfer to a TEM grid.

3.4 Transferring to a TEM grid

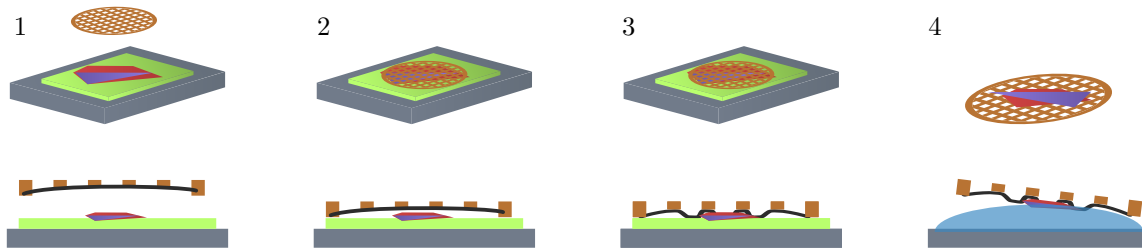


Figure 10: Schematic illustration of the transfer process. 1: A previously prepared heterostructure is located on the substrate and suitable TEM grid is placed on the substrate over the heterostructures with tweezers. 2: The TEM grid is held in place, for the samples transferred for this work the TEM grid was held in place by pressing a microscope slide onto the rim of the TEM grid with the stamping micromanipulator taking care in not pressing too hard as this will push the TEM grid into the PVA sealing the inside in such a way that the IPA cannot reach the inside. 3: After wetting the grid with a drop of IPA the resulting surface tension will hold onto the carbon film as the drop evaporates pulling it onto the PVA coated substrate and heterostructure. 4: After all the IPA has evaporated and the glass slide is removed a single drop of distilled water is added to dissolve the PVA releasing the TEM grid and allowing it to float on the drop, ready to be picked up with tweezers.

Transfer of the heterostructure to a TEM grid was performed using a previously devised polymer assisted method [17], where a diced silicon wafer is coated using a polymer before stamping. The flakes are then stamped directly on the polymer coating in the same manner as described in the previous section before being covered with a TEM grid, application of a single drop of either water or IPA depending on the polymer used connects the flexible holey carbon film of the TEM grid with the polymer coating by means of surface tension as the drop evaporates. This "seals" the heterostructure in between the holey-carbon film and the polymer. Adding another drop, this time the solvent for the polymer, allows the flake held by the TEM grid and the grid itself to separate from the silicon substrate; allowing it to be picked up using tweezers. The process is illustrated in Figure 10. The authors of the previously cited paper demonstrated that both the use of PMMA and PVA are possible but require different solvents, acetone and water respectively. The heterostructures transferred for this thesis were stamped on a diced silicon wafer coated with ~ 100 nm thick PVA and were then annealed at 400 °C in vacuum as there was significant contamination present.

TODO: is this still accurate at the time of submission?

4 Advanced electron microscopy techniques to map moiré physics at the nanoscale; an electron microscope pixelated array detector.

4.1 Electron microscope pixel-array detector

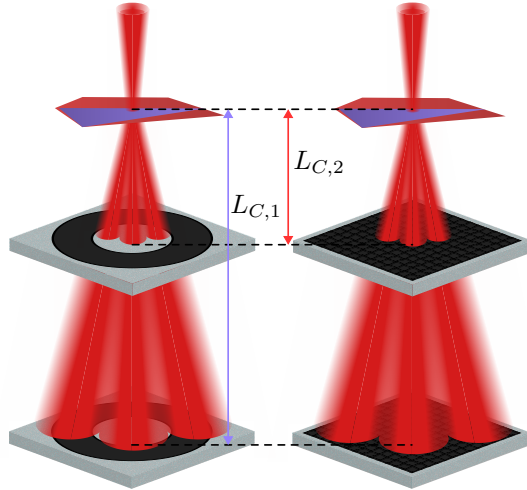


Figure 11: Figure schematically shows the difference between a monolithic fixed geometry high-angle annular dark field (HAADF) detector and a pixelated-array detector on the left- and right-hand side of the image respectively. As shown, the HAADF detector is only able to resolve features whose scattering diffracts the beam onto the monolithic annular detector. Since the Bragg angle is fixed for each feature, the signal can only be captured at a certain camera length. The HAADF detector is a single large punctured "pixel" that bunches all incident signals together. In contrast, the EMPAD is able to capture signals diffracted over a wider range of angles for every camera length as well as spatially separate the different signals, a HAADF and bright field detector could then be simulated by virtually masking and integrating the equivalent regions of the data after a measurement.

The electron microscope pixel-array detector, colloquially called the EMPAD for short, is as the name suggest a sensor for electron microscopes that consists of a grid of direct electron detecting pixels. Even though the EMPAD can be used in standard transmission electron imaging its strengths lie in scanning-TEM imaging due to the relatively little pixels but greater dynamic range of said pixels. In a scanning-TEM (STEM) mode the beam is cone-shaped and converges to a thin point-like spot that scans over the specimen, for small semi-convergence angles the zeroth order diffraction disk is a magnitude higher in intensity than the first order Bragg reflection disks. Since there is valuable information in the distribution of intensity in all disks its important that the detector has sufficient dynamic range to count individual electrons at all intensity ranges simultaneously using a high-gain per pixel charge integration circuit. The second major advantage of the EMPAD is the pixelated-array of detectors that, contrary to the regular monolithic annular dark field detectors, preserves the deflection angle information of the transmitted electron beams. Traditionally, elastic scattering deflects the electrons from the optical axis onto one of the annular ring shaped detectors encircling the optical axis, these detectors are called the dark field detectors. These singular annular detectors have a fixed detector geometry that only captures signals at certain camera lengths when

diffracted beams are impinging on the detector, as schematically shown in Figure 11. The EMPAD solves this problem by measuring the whole convergent-beam electron-diffraction (CBED) pattern using a single fast-readout, high dynamic range pixel grid on which every pixels' electron dose is stored separately such that after acquisition of a complete STEM scan the bright- and dark-field detectors can be virtually recreated by integrating the electron dose using annular or circular masks on the data. The pixelated nature of the detector enables the precise computation of the intensity distribution of not only the whole CBED pattern but also within each diffraction disk within the CBED pattern, greatly improving the potential resolution by means of ptychography methods [18, 19] as well as enabling charge density analysis [20, 21, 22] and strain analysis [23, 24]. The EMPAD's sensor is made up of a grid of 128 by 128 pixels and will thus always image the CBED or NBED pattern at this resolution. Every pixel counts single electron charges and stores the count in a 32-bit number. The EMPAD is able to equal the field-of-view of the HAADF-detector with a maximum of 512 by 512 equally positioned scan points. A schematic showing the geometry of a measurement is given in Figure 12a where a scanning probe is shown to scan over a diamond shaped moiré unit cell creating a CBED pattern on the EMPAD's pixel-array sensor. Nine CBED patterns for differing probe positions are displayed in Figure 12b. By virtually masking and integrating the first-order Bragg reflections for every CBED pattern to a single electron count one is able to recover a virtual annular dark-field image.

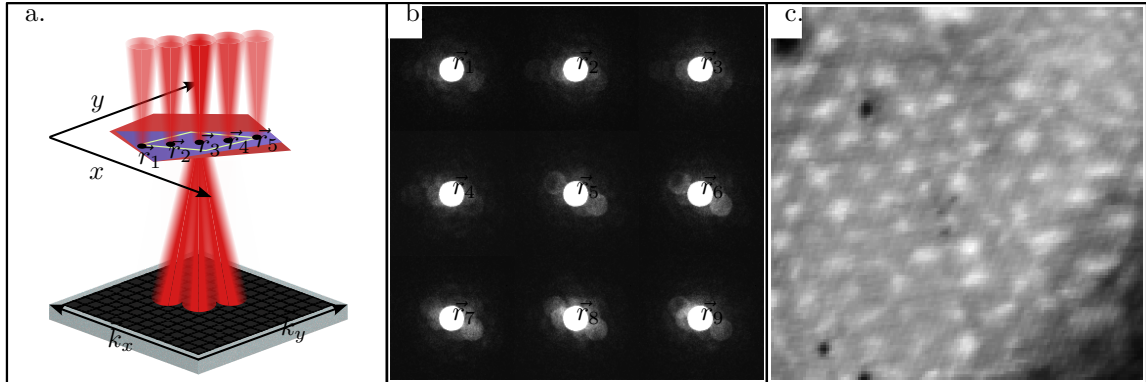


Figure 12: a) Schematic overview of an EMPAD measurement where a convergent electron beam probes the sample at positions \vec{r}_1 through \vec{r}_5 producing convergent-beam electron diffraction (CBED) pattern images of 128 by 128 pixels for each such position.b) Nine such CBED patterns imaged at different positions within a moiré cell using electric field measurement conditions.c) A virtual annular dark field image made by masking a thin annulus in the 4d-dataset. With only the first order Bragg reflections captured by the mask the atomic periodicity is visible within the image.

4.2 Strain analysis

Strain analysis in electron microscopy can be achieved through a multitude of ways, the main distinction between all of them is whether they are performed by analysing a real-space image captured by high-resolution TEM techniques or performed by analysing reciprocal space images captured through scanning-TEM techniques. An example of the first method is geometric phase analysis where displacements of atoms in a crystal are directly observed in the high-resolution image and strain can be computed [25, 26, 27]. The second method relies primarily on the fact that a

CBED/NBED pattern for a small enough convergent electron probe directly measures the local crystal structure. The reciprocal-space unit cell of the local crystal structure and thus the positions of the peak in the CBED pattern are directly correlated with the size of the real-space unit cell such that a compressing force in the real-space unit cell will elongate the reciprocal-space unit cell in the same direction and vice-versa for a tensile strain [24, 28, 29, 23], tracking the peaks then gives access to the strain information. In the following sections the second method will be applied for both large and small field-of-views.

4.2.1 Micrometer field-of-view strain analysis

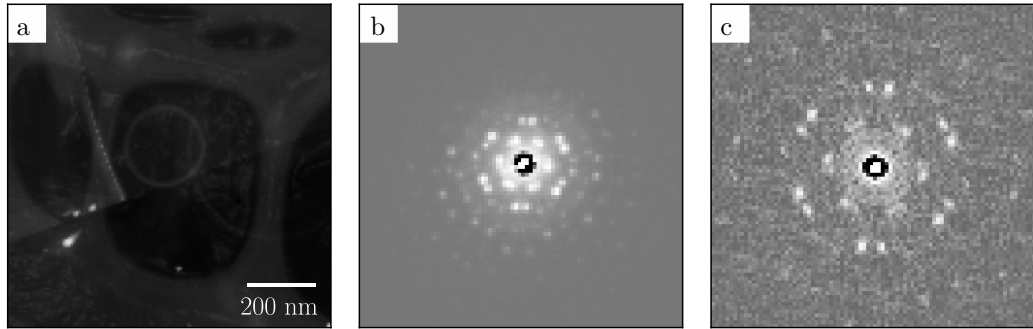


Figure 13: **a)** virtual annular dark-field image reconstructed by masking the dataset such that the detector geometry is equivalent to that of the HAADF-detector. Image is taken at the transition region of monolayer $MoSe_2$ (bottom) to a heterostructure of $MoSe_2$ and WSe_2 (top) on a lacy carbon grid. The faint circles in the middle of the image are contamination from inspection in TEM mode. Contamination in STEM mode caused the bright white spots on the left side of the image. **b)** logarithm of the nanobeam electron-diffraction pattern captured in the heterobilayer region of the image in **a**. Two sets of six diffraction disks, one set of six for each material, can be seen in the pattern. Due to local tilt of the crystalline layers diffraction disks on one side of the central 000-disk, in this case the bottom, are brighter than disks on the opposing side. **c)** Exit-wave power cepstrum (EWPC) transform of the NBED pattern displayed in **b**. The EWPC pattern does not suffer from unequal intensity distributions. Peaks in the pattern are distinguishable in the EWPC transform.

4.2.2 Nanometre field-of-view strain analysis

4.3 Ptychography

4.4 Charge density analysis

5 Case study of $MoSe_2/WSe_2$ moiré heterostructures

5.1 Verification of moiré pattern and its parameters

5.2 Analysis of in-plane strain

References

- [1] E. G. van Putten, D. Akbulut, J. Bertolotti, W. L. Vos, A. Lagendijk, and A. P. Mosk, “Scattering lens resolves sub-100 nm structures with visible light,” *Phys. Rev. Lett.*, vol. 106, p. 193905, May 2011.
- [2] C. Kisielowski, B. Freitag, M. Bischoff, H. van Lin, S. Lazar, G. Knippels, P. Tiemeijer, M. van der Stam, S. von Harrach, M. Stekelenburg, and et al., “Detection of single atoms and buried defects in three dimensions by aberration-corrected electron microscope with 0.5-Å information limit,” *Microscopy and Microanalysis*, vol. 14, no. 5, p. 469477, 2008.
- [3] D. B. Williams and C. B. Carter, *Transmission electron microscopy*. New York, NY: Springer, 2 ed., Jan. 2009.
- [4] “Field-emission electron gun, fe electron gun: Glossary: Jeol ltd..”
- [5] A. Eftekhari, “Tungsten dichalcogenides (ws₂, wse₂, and wte₂): materials chemistry and applications,” *J. Mater. Chem. A*, vol. 5, pp. 18299–18325, 2017.
- [6] A. Splendiani, L. Sun, Y. Zhang, T. Li, J. Kim, C.-Y. Chim, G. Galli, and F. Wang, “Emerging photoluminescence in monolayer mos₂,” *Nano Letters*, vol. 10, no. 4, pp. 1271–1275, 2010. PMID: 20229981.
- [7] O. Lopez-Sanchez, D. Lembke, M. Kayci, A. Radenovic, and A. Kis, “Ultrasensitive photodetectors based on monolayer MoS₂,” *Nature Nanotechnology*, vol. 8, pp. 497–501, June 2013.
- [8] B. Radisavljevic, A. Radenovic, J. Brivio, V. Giacometti, and A. Kis, “Single-layer MoS₂ transistors,” *Nature Nanotechnology*, vol. 6, pp. 147–150, Jan. 2011.
- [9] E. C. Regan, D. Wang, E. Y. Paik, Y. Zeng, L. Zhang, J. Zhu, A. H. MacDonald, H. Deng, and F. Wang, “Emerging exciton physics in transition metal dichalcogenide heterobilayers,” *Nature Reviews Materials*, vol. 7, pp. 778–795, May 2022.
- [10] C. Kittel, *Introduction to solid state physics*. Brisbane, QLD, Australia: John Wiley and Sons (WIE), 7 ed., Oct. 1995.
- [11] K. S. Novoselov, Z. Jiang, Y. Zhang, S. V. Morozov, H. L. Stormer, U. Zeitler, J. C. Maan, G. S. Boebinger, P. Kim, and A. K. Geim, “Room-Temperature Quantum Hall Effect in Graphene,” *Science*, vol. 315, pp. 1379–1379, Mar. 2007.
- [12] Y. Kusaka, K.-i. Nomura, N. Fukuda, and H. Ushijima, “Microcontact patterning of conductive silver lines by contact inking and its layer-transfer mechanisms,” *Journal of Micromechanics and Microengineering*, vol. 25, p. 055022, May 2015.
- [13] R. Frisenda, Y. Niu, P. Gant, A. J. Molina-Mendoza, R. Schmidt, R. Bratschitsch, J. Liu, L. Fu, D. Dumcenco, A. Kis, D. P. De Lara, and A. Castellanos-Gomez, “Micro-reflectance and transmittance spectroscopy: A versatile and powerful tool to characterize 2D materials,” *Journal of Physics D: Applied Physics*, vol. 50, p. 074002, Feb. 2017.

- [14] Y. Niu, S. Gonzalez-Abad, R. Frisenda, P. Marauhn, M. Drüppel, P. Gant, R. Schmidt, N. Taghavi, D. Barcons, A. Molina-Mendoza, S. De Vasconcellos, R. Bratschitsch, D. Perez De Lara, M. Rohlfing, and A. Castellanos-Gomez, “Thickness-Dependent Differential Reflectance Spectra of Monolayer and Few-Layer MoS₂, MoSe₂, WS₂ and WSe₂,” *Nanomaterials*, vol. 8, p. 725, Sept. 2018.
- [15] A. Castellanos-Gomez, M. Buscema, R. Molenaar, V. Singh, L. Janssen, H. S. J. van der Zant, and G. A. Steele, “Deterministic transfer of two-dimensional materials by all-dry viscoelastic stamping,” *2D Materials*, vol. 1, p. 011002, Apr. 2014.
- [16] A. Castellanos-Gomez, M. Buscema, R. Molenaar, V. Singh, L. Janssen, H. S. J. van der Zant, and G. A. Steele, “Deterministic transfer of two-dimensional materials by all-dry viscoelastic stamping,” *2D Materials*, vol. 1, p. 011002, Apr. 2014.
- [17] J. Köster, B. Liang, A. Storm, and U. Kaiser, “Polymer-assisted TEM specimen preparation method for oxidation-sensitive 2D materials,” *Nanotechnology*, vol. 32, p. 075704, Feb. 2021.
- [18] T. J. Pennycook, A. R. Lupini, H. Yang, M. F. Murfitt, L. Jones, and P. D. Nellist, “Efficient phase contrast imaging in STEM using a pixelated detector. Part 1: Experimental demonstration at atomic resolution,” *Ultramicroscopy*, vol. 151, pp. 160–167, Apr. 2015.
- [19] H. Yang, T. J. Pennycook, and P. D. Nellist, “Efficient phase contrast imaging in STEM using a pixelated detector. Part II: Optimisation of imaging conditions,” *Ultramicroscopy*, vol. 151, pp. 232–239, Apr. 2015.
- [20] J. A. Hachtel, J. C. Idrobo, and M. Chi, “Sub-Ångstrom electric field measurements on a universal detector in a scanning transmission electron microscope,” *Advanced Structural and Chemical Imaging*, vol. 4, p. 10, Dec. 2018.
- [21] Y. Wen, S. Fang, M. Coupin, Y. Lu, C. Ophus, E. Kaxiras, and J. H. Warner, “Mapping 1D Confined Electromagnetic Edge States in 2D Monolayer Semiconducting MoS₂ Using 4D-STEM,” *ACS Nano*, vol. 16, pp. 6657–6665, Apr. 2022.
- [22] S. Fang, Y. Wen, C. S. Allen, C. Ophus, G. G. D. Han, A. I. Kirkland, E. Kaxiras, and J. H. Warner, “Atomic electrostatic maps of 1D channels in 2D semiconductors using 4D scanning transmission electron microscopy,” *Nature Communications*, vol. 10, p. 1127, Mar. 2019.
- [23] Y. Han, K. Nguyen, M. Cao, P. Cueva, S. Xie, M. W. Tate, P. Purohit, S. M. Gruner, J. Park, and D. A. Muller, “Strain Mapping of Two-Dimensional Heterostructures with Subpicometer Precision,” *Nano Letters*, vol. 18, pp. 3746–3751, June 2018.
- [24] C. Ophus, “Four-Dimensional Scanning Transmission Electron Microscopy (4D-STEM): From Scanning Nanodiffraction to Ptychography and Beyond,” *Microscopy and Microanalysis*, vol. 25, pp. 563–582, June 2019.
- [25] M. Hÿtch, E. Snoeck, and R. Kilaas, “Quantitative measurement of displacement and strain fields from HREM micrographs,” *Ultramicroscopy*, vol. 74, no. 3, pp. 131–146, 1998.
- [26] M. J. Hÿtch, “GEOMETRIC PHASE ANALYSIS OF HIGH RESOLUTION ELECTRON MICROSCOPE IMAGES,”

- [27] L. Nguyen, H.-P. Komsa, E. Khestanova, R. J. Kashtiban, J. J. P. Peters, S. Lawlor, A. M. Sanchez, J. Sloan, R. V. Gorbachev, I. V. Grigorieva, A. V. Krasheninnikov, and S. J. Haigh, “Atomic Defects and Doping of Monolayer NbSe₂,” *ACS Nano*, vol. 11, pp. 2894–2904, Mar. 2017.
- [28] M. Van Winkle, I. M. Craig, S. Carr, M. Dandu, K. C. Bustillo, J. Ciston, C. Ophus, T. Taniguchi, K. Watanabe, A. Raja, S. M. Griffin, and D. K. Bediako, “Rotational and dilatational reconstruction in transition metal dichalcogenide moiré bilayers,” *Nature Communications*, vol. 14, p. 2989, May 2023.
- [29] N. P. Kazmierczak, M. Van Winkle, C. Ophus, K. C. Bustillo, S. Carr, H. G. Brown, J. Ciston, T. Taniguchi, K. Watanabe, and D. K. Bediako, “Strain fields in twisted bilayer graphene,” *Nature Materials*, vol. 20, pp. 956–963, July 2021.

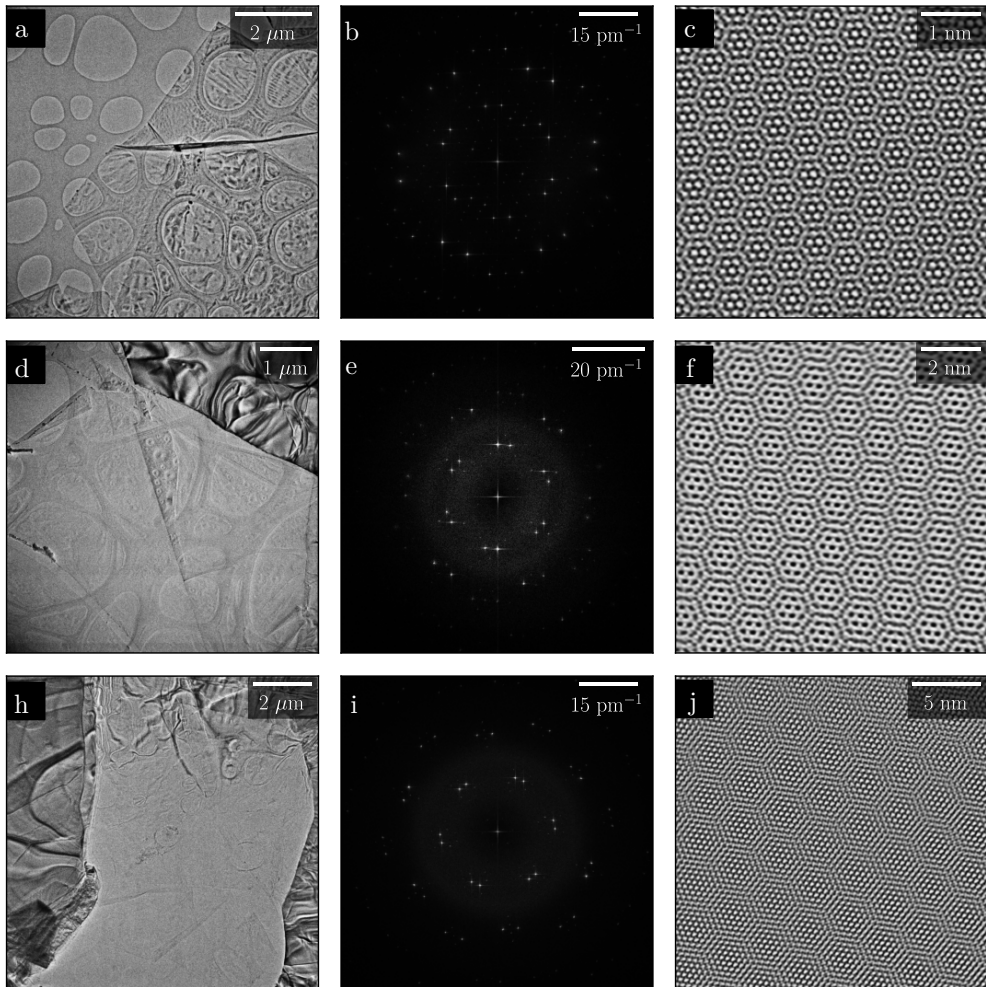


Figure 14: (a, d, h) HR-TEM images of three different $\text{MoSe}_2/\text{WSe}_2$ -Moiré heterostructures stamped under different angles verified by the FFT of images (b, e, i) taken at $460k\times$ magnification (not shown). The Moiré angle can be determined by measurement of the angle in between the two diffraction peaks in a set, for b, e, i the angle was measured to be 16.6° , 12.2° , and, 8.3° respectively. (c, f, j) displaying a reconstruction of filtered diffraction patterns, showing a clear Moiré superlattice. The Moiré superlattice cell was measured to be 0.47 nm , 1.06 nm , and, 1.69 nm ; for c, f, and, j. (a) The two layers of material show a rough surface that seems to arise during or after transfer to the TEM grid.

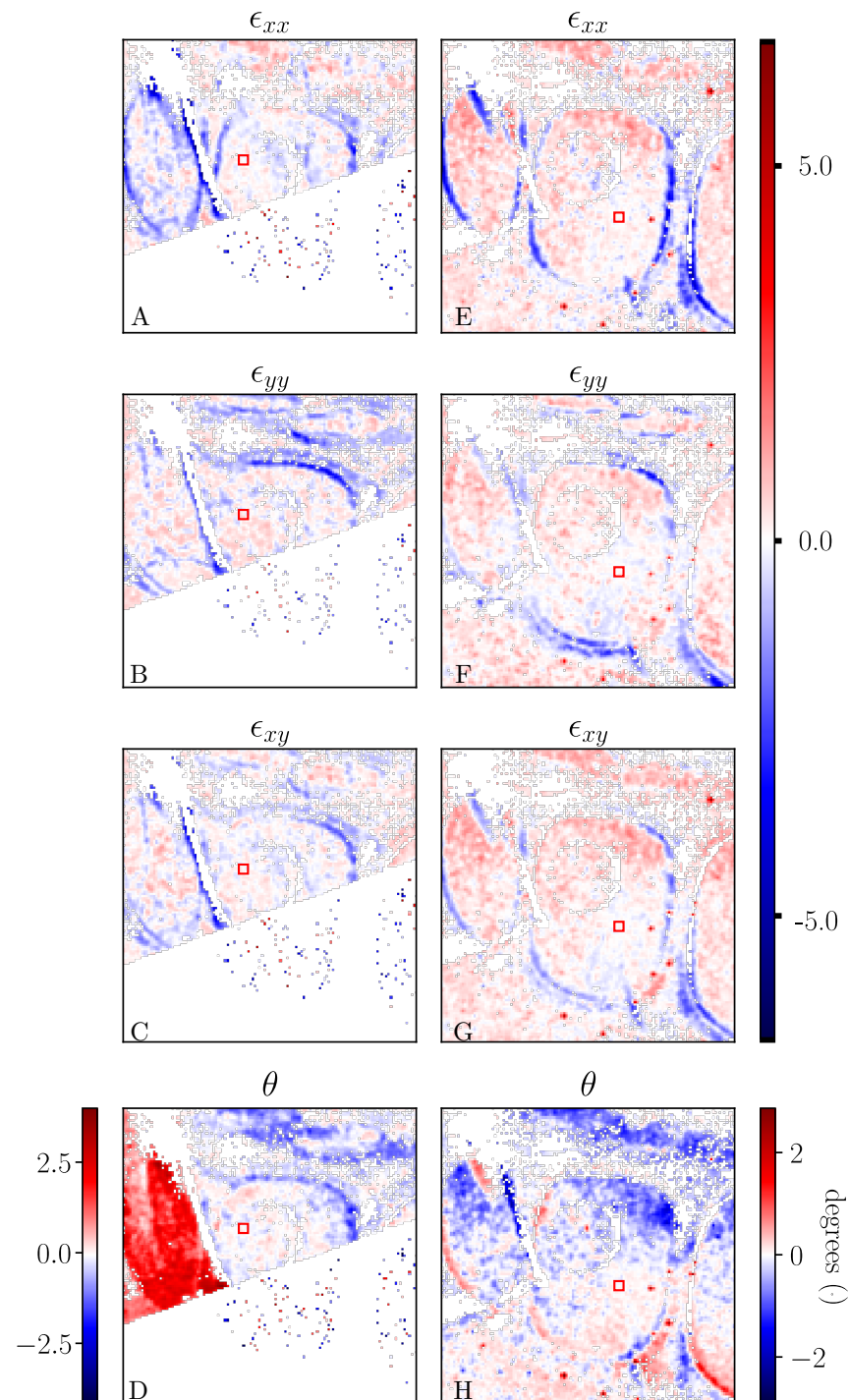


Figure 15: Overview of the global strain present in the heterostructure